Dynamic Preconditioning of the Minimum September Sea-Ice Extent

JAMES WILLIAMS AND BRUNO TREMBLAY[a]

Department of Atmospheric and Oceanic Sciences, McGill University, Montreal, Quebec, Canada

ROBERT NEWTON

Lamont-Doherty Earth Observatory of Columbia University, Palisades, New York

RICHARD ALLARD

Naval Research Laboratory, Stennis Space Center, Hancock County, Mississippi

(Manuscript received 23 July 2015, in final form 13 May 2016)

ABSTRACT

There has been an increased interest in seasonal forecasting of the Arctic sea ice extent in recent years, in particular the minimum sea ice extent. Here, a dynamical mechanism, based on winter preconditioning, is found to explain a significant fraction of the variance in the anomaly of the September sea ice extent from the long-term linear trend. To this end, a Lagrangian trajectory model is used to backtrack the September sea ice edge to any time during the previous winter and quantify the amount of sea ice advection away from the Eurasian and Alaskan coastlines as well as the Fram Strait sea ice export. The late-winter anomalous sea ice drift away from the coastline is highly correlated with the following September sea ice extent minimum ($r = -0.66$). It is found that the winter mean Fram Strait sea ice export anomaly is also correlated with the minimum sea ice extent the following summer ($r = -0.74$). To develop a hindcast model of the September sea ice extent—which does not depend on a priori knowledge of the minimum sea ice extent—a synthetic ice edge initialized at the beginning of the melt season (1 June) is backtracked. It is found that using a multivariate regression model of the September sea ice extent anomaly based on ice export from the peripheral Arctic seas and Fram Strait ice export as predictors reduces the error by 38%. A hindcast model based on the mean December–April Arctic Oscillation index alone reduces the error by 24%.

1. Introduction

There has been a negative trend in the Arctic Ocean sea ice extent since the late 1970s, when satellite observations became available on a consistent basis (Parkinson et al. 1999). This trend is present in all months and ranges from -0.30 to $-0.87 \times 10^6\,\mathrm{km^2\,decade^{-1}}$ (from -2.3% to $-13.6\%\,\mathrm{decade^{-1}}$) in May and September, respectively (Fetterer et al. 2002, updated daily). The rate of decline in the September minimum sea ice extent (SIE) accelerated in recent decades when compared to the 1978–96 time period (Comiso et al. 2008). Following the record minimum September SIE in 2012, the September sea ice extent recovered $1.5 \times 10^6\,\mathrm{km^2}$ in 2013, highlighting the significant amplitude of the interannual variability (Fetterer et al. 2002, updated daily).

The current decline of the September minimum sea ice cover is also accompanied by a decrease in mean sea ice thickness (Kwok and Rothrock 2009). During the period 1986–94, a mean reduction of draft depth of 1.5 m was observed from repeated submarine transects between the coast of Alaska and the North Pole. The decrease in sea ice draft is attributed primarily to sea ice dynamics with thermodynamics playing a less influential role (Tucker et al. 2001). The particular dynamical mechanisms leading to the reduction in thickness are an anomalously weak Beaufort Gyre, a broad Transpolar Drift Stream, and

[a] Additional affiliation: Lamont-Doherty Earth Observatory of Columbia University, Palisades, New York.

Corresponding author address: James Williams, Department of Atmospheric and Oceanic Sciences, McGill University, Montreal, QC H3A0B9, Canada.
E-mail: james.williams@mail.mcgill.ca

DOI: 10.1175/JCLI-D-15-0515.1

high export of multiyear ice (MYI) associated with a positive Arctic Oscillation (AO) index in the late 1980s and early 1990s. Likewise, Rigor and Wallace (2004) document a reduction in mean sea ice age during the same time period, associated with the sustained positive phase of the AO. In the mid-1990s, the AO returned to a more neutral state, yet the rate of decline of the September sea ice extent accelerated. Many studies build on this link between the AO and the MYI mass budget (Rigor and Wallace 2004), highlighting the importance of winter sea ice dynamical processes in the Arctic (e.g., Wang et al. 2009; Stroeve et al. 2011).

Of particular interest are the record September SIE minima in 2007 and 2012 with area losses of 36% and 48% of the mean 1979–2006 minimum sea ice extent, respectively (Fetterer et al. 2002, updated daily). The year-to-year ice loss leading to both of these minima are the largest observed during the satellite era. Summertime thermodynamic processes also play an important role in setting the September sea ice edge. In particular, the surface albedo feedback can significantly amplify an initial anomaly in open water area at the beginning of the melt season (Perovich et al. 2007). Perovich et al. (2008) propose that this mechanism was influential in the extensive loss of sea ice in the Beaufort Sea in 2007. Recently, Hutchings and Perovich (2015) showed that wintertime sea ice divergence as calculated from buoy triads in a region of approximately 1000 km^2 in the Beaufort Sea could account for the anomalously high local basal melt in 2007.

First year ice (FYI) is flatter than MYI and tends to be covered by lower-albedo melt ponds (Perovich and Polashenski 2012). This is another positive feedback, one that will become more important as the pack transitions to a seasonal ice cover. The continued loss of sea ice area in turn increases the heat content in the upper ocean. The anomalous oceanic heat can also be advected, affecting the subsequent basal melt of sea ice (Steele et al. 2010). In the western Arctic, open water anomalies early in the melt season can be caused by an anomalous oceanic heat flux through Bering Strait (e.g., Woodgate et al. 2010) as well as wind-driven divergence in the Chukchi and Beaufort Seas (e.g., Frey et al. 2015). Finally, Rigor et al. (2002) suggest that open water anomalies early in the melt season can be caused by divergent wind forcing along the Eurasian coastline during the previous winter associated with a positive phase of the AO.

Nikolaeva and Sesterikov (1970) find that FYI forming after 1 February in the Laptev Sea is unlikely to survive the following summer melt season. Based on this concept, Nikolaeva and Sesterikov (1970) developed and validated a skillful operational sea ice prediction system for the Laptev Sea. Following the same line of argument, Chevallier and Salas-Mélia (2012) showed that the ice fraction in the 0.9–1.5-m thickness category from a numerical model gives the largest predictive skill for a 4-month seasonal forecast of the minimum SIE. This thickness range is in line with that of Nikolaeva and Sesterikov (1970), who estimate that new ice forming on 1 February will be 1.15–1.45 m thick at the onset of melt.

Holland and Stroeve (2011) documented a change in the correlation between the simulated winter ice thickness, summer large-scale atmospheric circulation, and the minimum SIE as the pack ice transitioned from a perennial to a seasonal ice cover. In particular, they showed an increase in the correlation between the wintertime thin ice fraction and the minimum SIE from 0.3 in the late twentieth century to 0.65 in the middle of the twenty-first century. During the same time period, the correlation between the mean summer sea level pressure and the minimum SIE decreases from 0.5 to 0.1. This increase in the relative importance of winter processes suggests potential predictability of the minimum SIE on seasonal time scales as the sea ice thins.

With the opening of the summer pack ice in 2007, there has been an increased interest in short-term and seasonal forecasting of sea ice conditions, and in particular the minimum sea ice extent. This is exemplified by the creation of the Sea Ice Outlook, managed by the Sea Ice Prediction Network (https://www.arcus.org/sipn/sea-ice-outlook). The Sea Ice Outlook is an ongoing comparison of different methods used to forecast the minimum SIE. In the Sea Ice Outlook, many participants use numerical ice models forced with atmospheric fields from reanalyses. Other methods in use include statistical models and heuristic or mixed approaches. Short-term and seasonal forecasts however are notoriously difficult with the interannual variability of the September SIE showing no autocorrelation with the previous year (Serreze and Stroeve 2015). For instance, Stroeve et al. (2014) show that the collective skill in forecasting the September sea ice minimum is high in years when the minimum SIE is close to the long-term linear trend, while the collective skill is low in years when the September sea ice minimum falls far from the long term trend (e.g., the record low SIE minimum of 2012 or the anomalously high SIE minimum of 2013). This is in accord with Lindsay et al. (2008), who show that the lagged correlations between the North Atlantic Oscillation (NAO), the AO, or predictors from numerical simulations and the September SIE minimum greatly increase when the long-term trend in the SIE is not removed.

Following Nikolaeva and Sesterikov (1970), we use a Lagrangian back-trajectory framework to study the

dynamic preconditioning effect of sea ice export from the Alaskan and Eurasian peripheral seas into the central Arctic Ocean and sea ice export from the Arctic through Fram Strait on the September minimum sea ice extent. We use the results of this analysis to test a variety of hindcast models to predict the September minimum sea ice extent on a seasonal time scale. We focus on the time period 1993–2014, when the winter pack ice is thinner and responds more readily to wind forcing following the decline in MYI thickness during the late 1980s and early 1990 (Rigor and Wallace 2004; Tucker et al. 2001).

2. Data

In this study we use weekly averaged sea ice velocities from the Polar Pathfinder Daily Sea Ice Motion Vectors, version 3 (Tschudi et al. 2016). This dataset provides sea ice velocities interpolated onto the 25-km resolution Equal Area Scalable Earth (EASE) grid (Brodzik et al. 2012) with daily temporal resolution from 31 October 1978 until 31 December 2014. The sea ice velocity is calculated from the optimal interpolation (Fieguth et al. 1995) of satellite-derived sea ice drifts, buoy drifts, and free drift estimates calculated from NCEP–NCAR reanalysis geostrophic winds using a simple linear relationship between the ice drift and the wind speed (Thorndike and Colony 1982). The final gridded velocity product is computed as a weighted average of all data sources, where the weight is a function of the error attributed to each respective data source (Tschudi et al. 2016).

The satellite data incorporated in the Polar Pathfinder dataset are the Scanning Multichannel Microwave Radiometer (SMMR), onboard NASA's *Nimbus-7* satellite and operating from October 1978 until July 1987; the Special Sensor Microwave/Imager (SSM/I), onboard U.S. Defense Meteorological Satellite Program satellites and operating from July 1987 through the end of 2006; the Special Sensor Microwave Imager and Sounder (SSMIS), also onboard the U.S. Defense Meteorological Satellite Program satellites and operating from the beginning of 2007 until present; the Advanced Very High Resolution Radiometer (AVHRR), onboard the NOAA satellites and operating from July 1981 through the end of 2004; and the Advanced Microwave Scanning Radiometer–Earth Observing System (AMSR-E), onboard the still active NASA *Aqua* satellite and operating from June 2002 until August 2011. The spatial resolutions are 25, 25, 12.5, and 1.1 km for the SMMR, SSMI 37-GHz, AMSR-E, and AVHRR sensors, respectively. The root-mean-square error (RMSE) attributed to each data source is 5.1, 3.5, 3.3, 6.1, and less than 1 cm s^{-1} for SSMI, AMSR-E, AVHRR, free-drift estimates, and buoys respectively. An interpolation of all data sources excluding the buoys indicates an RMSE of 3.4 cm s^{-1} taking the Lagrangian buoy velocities to be the truth (Tschudi et al. 2016). In the summer, the satellite sensors have difficulties distinguishing surface ice features due to surface melt. As a result, the dataset relies more heavily on buoy data and the free-drift estimates. Nevertheless, the error in the monthly mean velocities from the gridded Polar Pathfinder sea ice velocity product during the summer (May–July) were found to be approximately 1.5 cm s^{-1} when compared with sea ice velocities derived from synthetic aperture radar (SAR) imagery (Sumata et al. 2015). Finally, a low bias in the SMMR velocity data was recently reported on the NSIDC website (see http://nsidc.org/data/docs/daac/nsidc0116_icemotion/smmr_ssmi.html). All analysis using satellite-derived sea ice velocities presented in this paper begin in 1993 and therefore the bias in the SMMR data does not affect the results presented below.

We use the NOAA–NSIDC Climate Data Record of Passive Microwave Sea Ice Concentration, version 2 (Meier et al. 2013, updated 2015). Sea ice concentration and extent from SMMR and SSMI (and SSMIS) 18-, 19-, and 37-GHz channels are given on a 25-km resolution grid. The physical SSMI sensors changed during the time series due to satellite replacements. Sensor recalibration was conducted during any overlap period between the sensor systems in order to minimize error in measured sea ice variables. Error estimates during sensor overlap are assessed to be smaller than 0.05% (Cavalieri et al. 1999; Eisenman et al. 2014).

3. Methodology

We use a Lagrangian ice trajectory model to quantify the amount of ice export from the Alaskan and Eurasian peripheral seas prior to the minimum sea ice extent in mid-September. This coastal export is largely associated with localized offshore winds resulting in polynyas, particularly in the Laptev Sea (Timohkov 1994). Southerly winds in the eastern Siberian, Chukchi, and Beaufort Seas, however, can be associated with cold air advection and anomalous sea ice growth lessening the effect of offshore sea ice motion. A simple scale analysis shows that dynamics is dominant in local sea ice thickness changes on short time scales. For instance, a typical ice speed of 5 cm s^{-1} toward the north will result in an ~5-km band of open water along the coast in one day, while a 5°C change in ice surface temperature due to cold (or warm) air advection will change the ice thickness by approximately 3 mm in one day for a 1-m-thick ice floe (from a simple 0-layer thermodynamic approximation assuming a

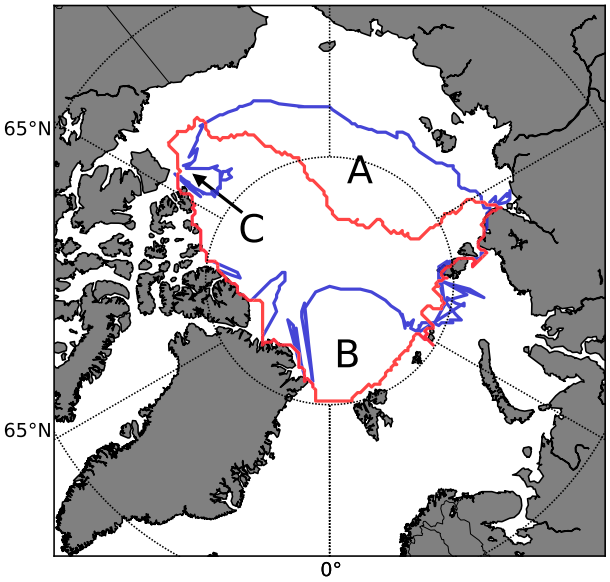

FIG. 1. Lagrangian trajectories of the 2007 minimum sea ice extent (red curve), and the 1 Nov 2006 position of the following September minimum sea ice edge (blue curve). The difference between area A (sea ice retreat) and area C (sea ice advance) is the dynamic preconditioning area (DPA). Area B is the Fram Strait export area (FSEA).

linear internal temperature profile). We note that the open water formed by advection will refreeze, resulting in approximately 10 cm of ice growth during the first day.

Our model tracks the sea ice edge back in time (time step = 1 week) from its position in September to any previous time. In the following, we refer to this imaginary line as, for instance, ''the June location of the September minimum sea-ice edge.'' In doing this, we ensure that ice is always present along the back trajectories, and that no trajectory ends prematurely in water due to errors in the satellite-derived drift velocities and concentrations. We then calculate the change in area between consecutive weeks during the backtracking procedure. This change in area is purely dynamic in nature and is associated with the advection of ice during the backtracking time period. The mean error of a trajectory is 13 km after a back-trajectory period of one month, and 83 km after a back-trajectory period of one year [see DeRepentigny et al. (2016) for details]. Note that the random errors in the individual trajectories tend to cancel as we calculate the net change in area over a longer time period.

Three closed polygons emerge from this exercise (Fig. 1). The difference in surface area between polygons A and C represents the net sea ice exported from the source region of the transpolar drift stream (TDS), while the surface area of polygon B represents the Fram Strait export area (FSEA). Polygons A, B, and C are readily identifiable in all years. The area enclosed by the September minimum sea ice extent (red contour) is largely balanced by the area enclosed within the backtracked contour (blue contour) or area A − area C ≈ area B. That is, to first order, the area of ice exported from the Eurasian peripheral seas (e.g., Timohkov 1994; Reimnitz et al. 1994; Alexandrov et al. 2000; Rigor et al. 2002; Krumpen et al. 2013) is of the same order of magnitude as the Fram Strait sea ice export (e.g., Rigor et al. 2002; Kwok 2009; Smedsrud et al. 2011). The departure from this first-order balance is the net divergence within the perennial Arctic pack ice. This can be shown by a simple application of the divergence theorem. In the following, we refer to the difference in surface area between areas A and C as the dynamic preconditioning area (DPA). The DPA is therefore the net area of ice exported from the Arctic peripheral seas into the central Arctic as demarcated by the backtracked contour (area A − area C). All polygon analysis is computed using the University of Manchester General Polygon Clipper library (http://www.cs.man.ac.uk/~toby/alan/software/).

To study the impact of interannual variability in dynamic preconditioning on the sea ice extent, we first detrend the DPA and FSEA. To this end we calculate the ''weekly DPA'' by backtracking the ice edge from one week to the prior from the time of the September minimum to 1 November of the previous year for all years between 1993 and 2014. We calculate the linear trend for each individual week, and subtract the appropriate trend line from each weekly DPA to form the weekly DPA anomaly. This procedure filters out both the average seasonal cycle and the long-term trend, highlighting the interannual variability.

4. Results

a. *Backtracking the September SIE*

The correlation between the weekly DPA and FSEA anomaly, integrated from the week of the SIE minimum to each prior week, and the anomaly of the September SIE minimum are computed for the 1993–2014 period. The sea ice export from the peripheral seas of the Arctic as measured by the integrated DPA anomaly is well correlated to the anomalous September SIE (Fig. 2). For the summer months, the correlation ($r = -0.45$) between the integrated DPA anomaly and the SIE minimum anomaly (Fig. 2, black curve) is the result of open water created dynamically. Open water can be created directly by ice export through Fram Strait and/or compaction of sea ice within the Arctic Ocean or indirectly through thermodynamic feedback mechanisms. In this

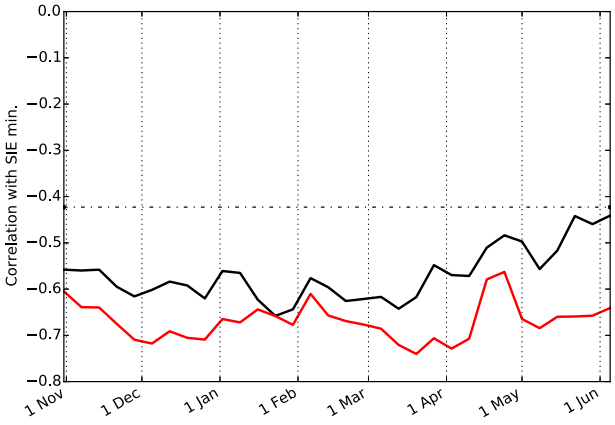

FIG. 2. Correlation between the anomaly of the September SIE minimum and the DPA (black) and FSEA (red) integrated from September to a prior time t on the x axis. All time series were first detrended using a linear best fit calculated over the time period 1993–2014. The dash-dotted line is the 95% confidence level.

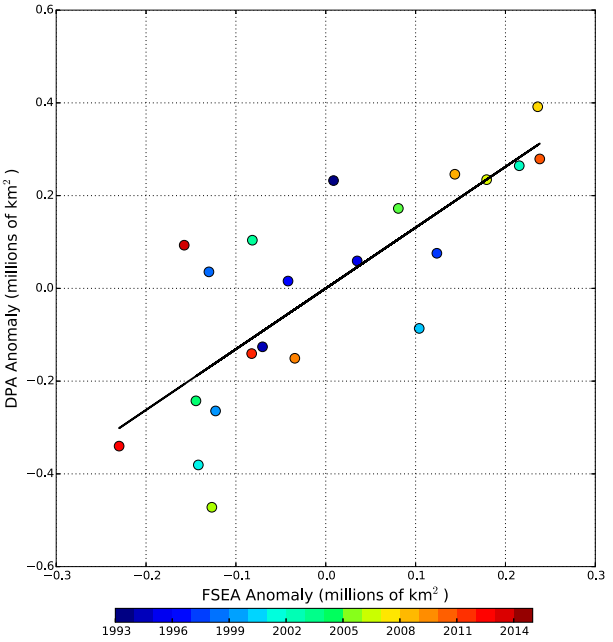

FIG. 3. Scatterplot of the anomalies of the FSEA and DPA integrated from November until June. The correlation coefficient is $r = 0.79$ and it is significant at greater than 99% confidence. Area anomalies are reported in units of millions of square kilometers.

paper, we do not attempt to assess the potential predictability of summer processes. In the late winter, the magnitude of the correlation increases ($r = -0.66$) until the third week of January. The integrated FSEA anomaly (Fig. 2, red curve) is also significantly correlated ($r \approx -0.7$) with the following September minimum SIE for all spring and winter months. That is, anomalously low minimum September SIE and anomalously high FSEA typically occur the same year.

The first-order sea ice area balance laid out above implies that the net DPA and FSEA are not independent time series. Furthermore, we find that the winter anomalies in FSEA and DPA are well correlated ($r = 0.79$) (Fig. 3). The anomalies in both variables are correlated with the phase of the December–April (DJFMA) AO index; $r = 0.55$ and $r = 0.59$ for the FSEA and DPA, respectively. This is because a positive AO is associated with deeper and more frequent penetration of cyclones in the eastern Arctic, which provide the wind forcing necessary to enhance the transpolar drift stream (Zhang et al. 2004). These correlations indicate a coherent transpolar drift stream strength anomaly during winter, with anomalous FSEA and anomalous export from the Eurasian peripheral seas occurring in the same years. During the summer months, the integrated anomalies of the FSEA and the DPA are not significantly correlated ($r = 0.31$). The summer integrated FSEA is small both compared to the integrated winter FSEA (Kwok 2009) and integrated summer DPA (results not shown). We find that the summer anomaly of FSEA is also small compared to the summer anomaly of DPA. This implies that the first-order balance discussed above breaks down during the melt season as the DPA is no longer compensated for by FSEA.

The correlation between the winter (DJFMA) mean AO index and the following September SIE anomaly is $r = -0.56$ (Fig. 4). One clear outlier is the year 2010. First, there was a large departure from the mean negative AO atmospheric circulation, with anomalously high advection of MYI from the Beaufort into the Chukchi Sea, where the long-term SIE decline is largest. Second, the Arctic mean ice volume was at a record low, creating unfavorable conditions for a high September SIE (Stroeve et al. 2011). Another outlier is 2014. During that year, the AO was positive and summer ice loss was large in the Laptev and Kara Seas (Fetterer et al. 2002, updated daily). The pack ice during the summer, however, was advected into the Barents Sea in August, resulting in an overall anomalously high September SIE in that region.

Note that the connection between the AO and minimum SIE is only present from 1993 onward, after the large MYI export from the Arctic during the late 1980s and early 1990s (Tucker et al. 2001; Rigor and Wallace 2004). Before that time, the phase of the AO did not significantly affect the variability in peripheral sea ice export on a pan-Arctic scale, presumably because the pack ice was on average thicker than at present. This increase in sea ice mobility in 1993 can also be seen in the results of Rampal et al. (2009), who show a strong positive anomaly in mean sea ice drift speed from buoy data between 1990 and 1994. For 1979–93, the

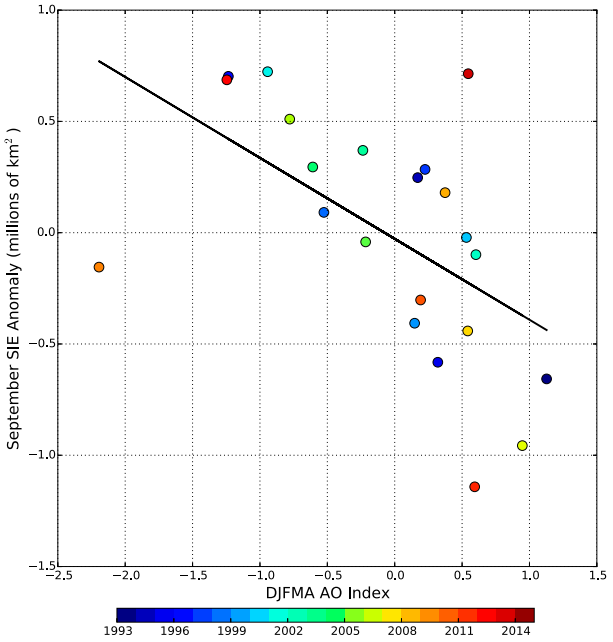

FIG. 4. Scatterplot of the winter mean AO (DJFMA) and the anomaly of the following September minimum SIE. The correlation coefficient is $r = -0.56$ and it is significant at greater than 99% confidence.

correlation ($r = -0.10$) between the wintertime AO (DJFMA) and the following September SIE anomaly is not statistically significant (not shown). This change in the nature of the correlation between the winter mean AO and minimum SIE in the early 1990s is robust whether we use two different linear trends for the time periods 1979–92 and 1993–2014, or if we fit an exponential decay to the September SIE time series. This result is in contrast with Holland and Stroeve (2011), who argue that the correlation between the detrended minimum SIE and the winter (January–April) mean AO is only marginally significant in recent years. The difference between our analysis and that of Holland and Stroeve (2011) is that they included 1979–92 when the correlation between the AO and the minimum SIE is not significant. Our results using the late winter DPA as a characterization of sea ice thickness in the Arctic peripheral seas are in line with their result showing the increasing importance of thin ice area on the September SIE anomaly.

Sea ice export from the Arctic peripheral seas can be accounted for by export from the Arctic predominantly through Fram Strait or by net convergence of the pack through ridging primarily in the region north of the Canadian Arctic Archipelago. Prior to 2007, the DPA is typically smaller than the FSEA (Fig. 5). This indicates that the perennial pack ice experienced net divergence during winter and spring. In other words, for 1993–2006, the area enclosed by the November position of the September SIE was smaller than the following September SIE [i.e., $(1/A)(dA/dt) > 0$, where A is the time-varying area enclosed by the backtracked September SIE contour; e.g., dA in Fig. 1 is the difference in area between the region enclosed by the blue curve and the region enclosed by the red curve]. Since 2007, the DPA has been larger than the FSEA, implying that the perennial pack ice has experienced net convergence. This is in accord with observations of the MYI cover north of the Canadian Arctic Archipelago that showed substantial sea ice convergence in the freezing season following the 2007 SIE minimum (Kwok and Cunningham 2012). The larger trend in the DPA, associated with a transition from net divergence to net convergence, indicates a substantially weaker ice pack in the central Arctic, as the magnitude of the integrated DPA between June and December has more than doubled in 20 years. The fact that both time series exhibit significant positive trends is evidence of the increasing mobility of the pack in recent decades in line with the findings from Rampal et al. (2009).

b. *Backtracking a synthetic ice edge*

We repeat the same analysis using a synthetic sea ice edge, since the location of the September sea ice extent is not known a priori at the beginning of June, when seasonal forecasts are typically issued. The synthetic ice edge studied here consists of the 77.5°N latitude band passing through the peripheral seas and the 80°N line across Fram Strait (see Fig. 6, dark red curve). We seed the back-trajectory model with points on the synthetic ice edge on 1 June and calculate their prior positions with a weekly temporal resolution until 1 November of the previous year as discussed in the previous section. The DPA and FSEA recalculated using the synthetic ice edge are again apparent in the backtracked trajectories (Fig. 6). This yields a new 22-yr time series of DPA and FSEA for each week (from June to November) of the 21-yr time series (1993–2014).

Again, we detrend the DPA and FSEA anomaly time series in the manner described above. We integrate from 1 June to any given prior week until 1 November and correlate with the minimum SIE (Fig. 7). We note a rapid increase in the magnitude of the correlation between the integrated DPA anomaly between June and April and the September SIE anomaly. The maximum correlation (in magnitude) is similar to that found from backtracking the September SIE (see previous subsection). The peak correlation however occurs two and a half months later in the spring when compared to the results from backtracking the September SIE. The timing and magnitude of the

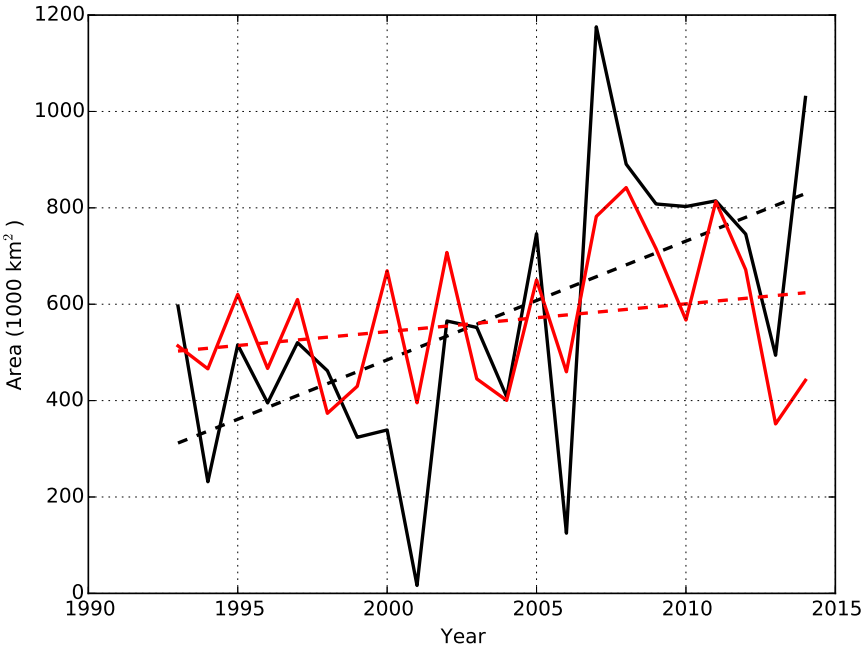

FIG. 5. Time series of the DPA (black) and FSEA (red) calculated using our Lagrangian back-trajectory model for the time period 1993–2014. The DPA and DFEA are integrated between the year's September SIE minimum and 1 November of the previous year. The dashed lines show the linear trend.

peak correlation are sensitive to the exact location used for the synthetic ice edge and the integration start date. In many years, the initial synthetic ice edge is far from the previously computed June position of the September SIE. This is likely to account for the disparity in correlation between the integrated DPA anomaly and the September SIE anomaly as seen in Figs. 2 and 7. On the other hand, the FSEA time series is robust with respect to the choice of the synthetic ice edge position because the synthetic ice edge is always defined across Fram Strait at 80°N.

The maximum correlation (in magnitude) between the integrated DPA—from 1 June to the third week of April—and the September SIE is $r = -0.58$ (Fig. 7). The maximum correlation (in magnitude) between the integrated FSEA—from 1 June to the third week of January—and the minimum SIE is $r = -0.72$ (Fig. 7). Note that the DPA and FSEA derived from the synthetic ice edge no longer depend on the future (unknown) location of the September SIE minimum and thus can be used in a predictive model. The slope of the best-fit lines for the period of maximum correlations (in magnitude) indicates that anomalies in the DPA or FSEA are amplified fivefold in the September SIE anomaly (Figs. 8a,b). This is likely due to feedback mechanisms (e.g., melt pond formation, open water heat absorption, greenhouse effect of warm liquid water clouds) associated with early melting out at the beginning of the melt season. Both the DPA and the FSEA anomalies computed from the synthetic sea ice edge remain well correlated with the winter mean AO index. In the following, we use the DPA anomaly integrated from the third week of April until 1 June, the

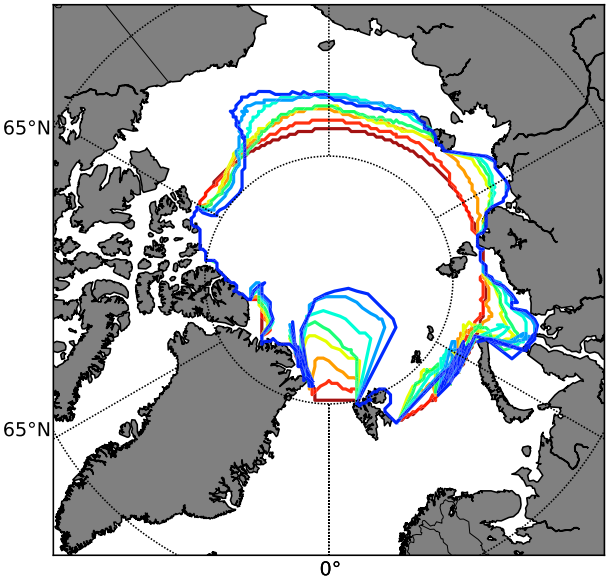

FIG. 6. Lagrangian trajectories of the synthetic ice-edge initialized 1 Jun 2007 (dark red curve); note that the synthetic ice edge is the 77.5°N latitude contour. The monthly backtracked position of the synthetic ice edge is shown in color, with the final curve being the 1 November position (blue).

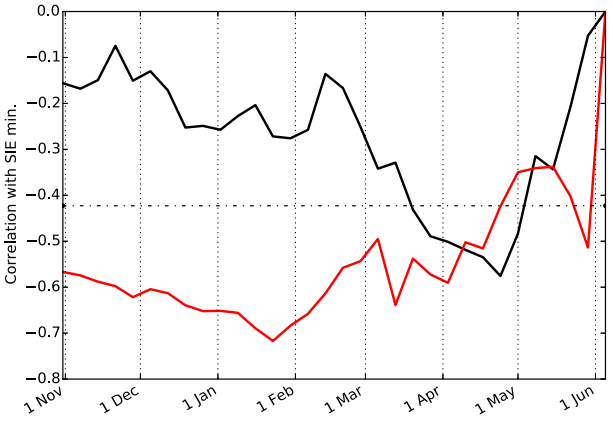

FIG. 7. Correlation between the anomaly of the September SIE minimum and the DPA (black) and FSEA (red) from the synthetic ice-edge integrated from 1 June to a prior time t on the x axis. All time series were first detrended using a linear best fit calculated over the time period 1993–2014. The dash-dotted line is 95% confidence level.

FSEA anomaly integrated from the third week of January until 1 June, and the winter (DJFMA) mean AO index as predictor variables in a hindcast model of the September SIE.

c. *Hindcast of the September minimum SIE*

We develop several hindcast models to estimate the minimum September SIE from 1993 to 2014. The simplest model, called H1, is the long-term linear trend of the September SIE, written as $\mathrm{SIE}_{\mathrm{pred}} = a_1 t + C$, where $\mathrm{SIE}_{\mathrm{pred}}$ is the predictand and a_1 and C are constants determined from a least squares fit. Three additional hindcast models (H2, H3, and H4) are formed by adding the individual effect of the DPA, FSEA, or AO to the previous model (H1) in order to predict the interannual variability of the September SIE. These models can be written mathematically as $\mathrm{SIE}_{\mathrm{pred}} = a_1 t + b_1 x_1 + C$, where x_1 is either the DPA anomaly, FSEA anomaly, or the AO (DJFMA) and again all constants are found from a least squares fit. Hindcast model H5 is formed by using both the DPA anomaly and FSEA anomaly to predict the interannual variability. This model can be written as $\mathrm{SIE}_{\mathrm{pred}} = a_1 t + b_1 x_1 + b_2 x_2 + C$, where x_1 is the DPA anomaly, x_2 is the FSEA anomaly, and all other symbols are as before. Finally, hindcast model H6 uses all three variables to predict the interannual variability and can be written as $\mathrm{SIE}_{\mathrm{pred}} = a_1 t + b_1 x_1 + b_2 x_2 + b_3 x_3 + C$, where x_3 is the winter (DJFMA) mean AO index and all other variables are as in H5.

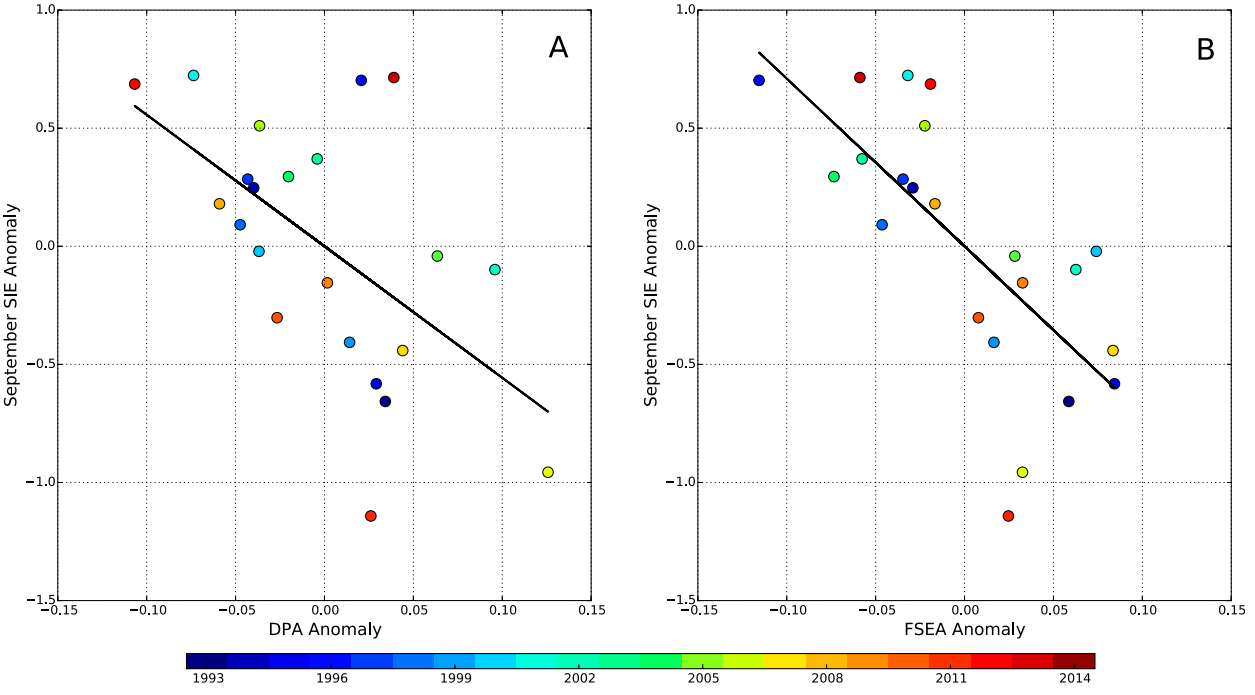

FIG. 8. Scatterplots of anomalies of (a) DPA and September SIE minimum, and (b) FSEA and September SIE minimum. The corresponding correlation coefficients are $r = -0.58$ in (a) and $r = -0.72$ in (b). Both correlations are significant at greater than 99% confidence. All areas reported are in units of millions of square kilometers. Note that DPA and FSEA are computed from backtracking the synthetic sea ice edge initialized at the beginning of the melt season (1 June) and then integrating the anomaly until the point of maximum correlation as seen in Fig. 7.

TABLE 1. Correlation coefficients (r^2), adjusted correlation coefficients ($\bar{r}^2$), and standard deviation of the hindcast error (σ_{err}) in units of millions of square kilometers for our six hindcast models of the September SIE from 1993 to 2012.

Label	Predictors	r^2	$\bar{r}^2$	σ_{err}
H1	Year	0.680	0.663	0.528
H2	Year, DPA	0.785	0.763	0.432
H3	Year, FSEA	0.844	0.828	0.367
H4	Year, AO	0.779	0.755	0.439
H5	Year, DPA, FSEA	0.875	0.854	0.330
H6	Year, DPA, FSEA, AO	0.882	0.854	0.320

As expected, increasing the number of predictors increases the correlation coefficient and decreases the error variance of the hindcast models (Table 1). We also compute the adjusted correlation coefficient ($\bar{r}^2$) to test if the increase in the correlation coefficient is statistically significant compared to the addition of a random variable to the model. The adjusted correlation coefficient increases from H1 through H5 and remains constant between H5 and H6. This indicates that including the winter mean AO into the model does not statistically improve the model for forecasting, but rather it results in an overfitting of the model to the hindcast data. The improvement from H1 to H5 is visually clear (Fig. 9) and quantifiable as a 38% reduction in the error variance when the interannual variability is predicted using the DPA anomaly and FSEA anomaly (as in H5). We also show H4 in Fig. 9 since it does not rely on the existence of the sea ice drift from the Polar Pathfinder dataset. Note that this product is not yet processed in near–real time and therefore cannot be used in an operational forecast model. H4 shows a 21% reduction in the error variance with respect to H1.

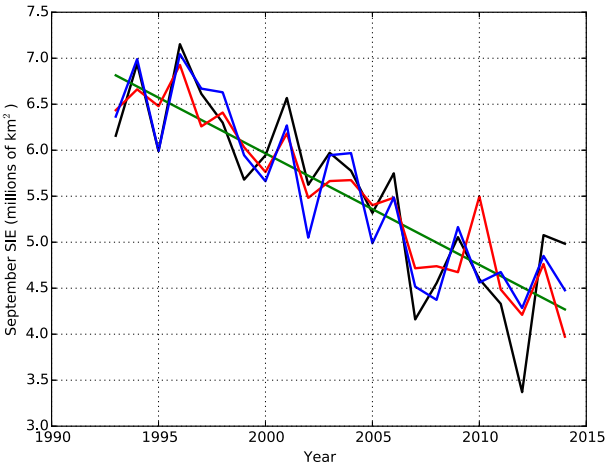

FIG. 9. Three prediction models of the observed September SIE (black) from 1993 to 2014: H1 (green), H4 (red), and H5 (blue). Table 1 shows the results of each hindcast model as well as the predictor variables used in each hindcast.

5. Discussion

We note that the correlations presented above are not proof of a physical mechanism, and direct attribution of the physical mechanism giving rise to these correlations would require analysis of a fully coupled model in which a complete energy and mass budget can be calculated. That said, we argue that the physical process that gives rise to these correlations is the enhanced generation of FYI during the late winter between the backtracked sea ice edge and the coastline, associated with a divergent sea ice drift field. The DPA region accounts for the sea ice area exported from peripheral seas of the Arctic into the central Arctic Ocean. This export is not compensated by an influx of ice through Bering Strait (e.g., Travers and Woodgate 2012). Therefore, there is in a net deficit in the sea ice area budget that must be compensated by FYI formation in order to maintain a fully ice-covered Arctic in winter (Fetterer et al. 2002, updated daily). In particular, we see large areas of DPA in many years along the Laptev Sea polynya, a region of high localized FYI formation (Rigor and Colony 1997; Dethleff et al. 1998). The timing of this FYI formation is important, with FYI formed from the third week of January through May giving rise to the highest correlation with the following September SIE. This is in accord with Nikolaeva and Sesterikov (1970), who find that sea ice forming in the Laptev Sea after 1 February is unlikely to grow thick enough to survive the following summer melt. This leads to an earlier melt onset in late spring and early summer allowing for the ice-albedo feedback to operate at a time when the sun is high above the horizon (Perovich et al. 2007). This is also observed in idealized coupled modeling experiments by Chevallier and Salas-Mélia (2012) showing that the thin ice fraction late in the winter is a good predictor for a seasonal forecast of the following September SIE.

We find that the integrated winter FSEA is of the same order as the integrated winter DPA. This is in accord with previous estimates of Eurasian peripheral sea ice export (e.g., Timohkov 1994; Reimnitz et al. 1994; Alexandrov et al. 2000; Rigor et al. 2002; Krumpen et al. 2013) and Fram Strait sea ice export (e.g., Rigor et al. 2002; Kwok 2009; Smedsrud et al. 2011). The implication is that a large fraction of the sea ice exported through Fram Strait is replaced by FYI along the Eurasian and Alaskan coastlines (Reimnitz et al. 1994). Furthermore, we find that the anomalous winter FSEA is strongly correlated with the anomalous winter DPA, indicating that the FSEA and the DPA covary on the interannual time scale.

Internal pack ice divergence during winter has been shown by Hutchings and Perovich (2015) to be an important factor for determining the following September minimum SIE, particularly in 2007. The FSEA (both in mean and anomaly) is largely balanced by the DPA with the departure from this balance being associated with perennial pack ice divergence. Therefore the FSEA accounts for both the first- and second-order processes that can each dynamically precondition the sea ice cover for anomalous September minimum SIE. Presumably, this is why we find the FSEA to be the best single predictor of the September SIE anomaly found in this study.

Rigor et al. (2002) show that the winter sea ice drift regressed on winter-mean AO is linked with the summer sea ice extent along the Eurasian coastline. We confirm this result with an independent method: the formation of the DPA region based on Lagrangian back-trajectory analysis. In addition we find that the timing of the thinning in the peripheral seas is important and that it is DPA formed after late January (Fig. 2), which is well correlated with the following September SIE. We find that the FSEA anomaly is better correlated with the September SIE anomaly than the DPA or the AO individually. This is in contrast with Rigor et al. (2002), who take the higher correlation between the September SIE and the AO index, as opposed to the NAO index, to be evidence of the greater importance of divergence in the eastern Arctic than the FSEA. We argue that the FSEA is a better predictor of the summer SIE because it provides a good estimate for the sum of the sea ice export from the peripheral seas and the net perennial pack ice divergence.

The dynamic processes during winter determine, to a large degree, which locations within the Arctic will have thicker sea ice at the onset of melt. Therefore, the sea ice thickness field is very important for initializing a numerical prediction model, such as those participating in the sea ice outlook. A perfect numerical forecast model initialized at the beginning of the melt season should in principle perform equally well on average as the methods shown here due to the predictive knowledge encoded in the initial conditions. The recently available thin sea ice thickness fields from the ESA's *Soil Moisture and Ocean Salinity (SMOS)* satellite (Tain-Kunze et al. 2014) and the upcoming sea ice thickness data from NASA's *Ice, Cloud and Land Elevation Satellite 2* (*ICESat-2*) satellite could allow for better initialization of numerical models, as well as the further study of the role of sea ice dynamics on the sea ice thickness distribution spatial and temporal evolution.

Studies of the sea ice energy budget prior to the onset of melt based on in situ data by Persson (2012) and Else et al. (2014) show that the local onset of melt is triggered by a reduction in the longwave radiation deficit at the ice surface. The surface longwave deficit is associated with the passing of synoptic weather systems resulting in increased downwelling longwave radiation due to cloud cover. This indicates potential for predictive skill of the localized melt onset date using observation of the synoptic weather conditions in the late May or early June. By incorporating predictors of the melt onset date in the model, a more skillful seasonal forecast of the minimum sea ice extent could be obtained. Prediction of the summer processes that are not influenced by the initial sea ice conditions at the beginning of the melt season is not currently possible (and may not be possible in general due to the chaotic nature of the atmospheric forcing). For example, Stroeve et al. (2014) show that ensemble predictions of the September minimum SIE issued on 1 July or 1 August do not statistically improve when compared with predictions made on 1 June.

Schröder et al. (2014) find that the most skillful predictor of the minimum sea ice extent is the area covered by melt ponds in a numerical sea ice model between 1 May and 25 June. In their study, including the melt pond area after 25 June decreases the predictive skill of the forecast. Liu et al. (2015), however, find that the predictive skill of a forecast of the September SIE based on a 12-yr time series of melt pond area from the Moderate Resolution Imaging Spectroradiometer (MODIS) increases significantly after 25 June and continues to increase until September. The uncertainty of the MODIS-derived melt pond area, however, is largely due to cloud masking as well as to difficulty distinguishing between thin ice and melt ponds (Rösel et al. 2012). We also note that many of the model pixels used in Schröder et al. (2014) that exhibit a significant correlation between the simulated melt-pond area coverage and the minimum sea ice extent are located in geographical areas that are outside of the seasonal ice zone. These include large areas of Baffin Bay, where ice is not present at the end of the melt season, and the central Arctic and Canadian Arctic Archipelago where ice is almost always present at end the of the melt season. We hypothesize that the melt-pond fraction at these points covaries with other factors that are important for the September sea ice extent. For instance, the first year ice areal extent in Baffin Bay at the onset of the melt season is correlated with the winter-mean NAO and AO (Deser et al. 2000).

6. Conclusions

We have run a Lagrangian back-trajectory model based on satellite-derived sea ice drifts for the years 1993–2014. From the back-trajectory analysis, we

compute time series of the dynamic preconditioning area (DPA) and the Fram Strait export area (FSEA). We have shown that the integrated winter anomaly of sea ice export from the peripheral seas of the Arctic as characterized by the DPA as well as the integrated winter FSEA anomaly are both significantly correlated to the following September SIE. We find that the DPA and FSEA are not independent time series and their anomalies are strongly correlated ($r = 0.79$). Both the FSEA and the DPA anomaly are correlated to the AO index during winter ($r = 0.55$ and $r = 0.59$, respectively). It follows that the winter mean AO index during this time period is also correlated to the following September SIE anomaly ($r = -0.56$). During the period 1979–92, we note the lack of a significant correlation between the AO and the September SIE anomaly because the sea ice cover was likely strong enough to resist the anomalous wind forcing associated with the phase of the AO.

We analyzed several hindcast models of the September SIE based on winter preconditioning of the pack. These models do not rely on a priori knowledge of the future conditions, as they are formed by backtracking a synthetic ice edge (located at 77.5°N) through winter. We find that a multivariate statistical model using the long-term trend, the DPA anomaly, and the FSEA anomaly provides the lowest RMSE ($0.33 \times 10^6\,km^2$) without overfitting to the observed September minimum SIE. This model would be available on 1 June giving a 3.5-month lead time before the September minimum SIE. Using the mean DJFMA AO index to characterize the interannual variability increases the RMSE ($0.43 \times 10^6\,km^2$) but adds a gain of one month in the forecast lead time. A regional or pan-Arctic forecast based on the FSEA or DPA as calculated above requires the real-time (or near real time) production of sea ice velocity vectors. We expect an observation-based seasonal forecast derived from the results presented could be used operationally with success.

Acknowledgments. James Williams is grateful to the North Slope Borough of Alaska for their financial support through the Eben Hopson Fellowship. James Williams was funded by the U.S. Naval Research Laboratory Oceanography Division during the summer of 2014 as part of the Naval Research Enterprise Internship Program (NREIP). Bruno Tremblay is grateful for financial support from the Office of Naval Research (N000141110977), the Canadian Sea Ice and Snow Evolution (CanSISE) Network funded by NSERC Climate Change and Atmospheric Research program and the NSERC Discovery program. Robert Newton is grateful for financial support by the Office of Naval Research (N000141110977). Richard Allard is funded under the NRL Core project (N0001416WX00044) Determining the Impact of Sea Ice Thickness on the Arctic's Naturally Changing Environment (DISTANCE). We thank Dr. Jennifer Hutchings and two anonymous reviewers whose thoughtful critiques and suggestions led to a significantly improved final manuscript.

REFERENCES

Alexandrov, V., T. Martin, J. Kolatschek, H. Eikcen, M. Kreyscher, and A. Makshtas, 2000: Sea ice circulation in the Laptev Sea and ice export to the Arctic Ocean: Results from satellite remote sensing and numerical modeling. *J. Geophys. Res.*, **105**, 17 143–17 159, doi:10.1029/2000JC900029.

Brodzik, M. J., B. Billingsley, T. Haran, B. Raup, and M. H. Savoie, 2012: Ease-grid 2.0: Incremental but significant improvements for Earth-gridded data sets. *ISPRS Int. J. Geoinf.*, **1**, 32–45, doi:10.3390/ijgi1010032.

Cavalieri, D. J., C. L. Parkinson, P. Gloersen, J. C. Comiso, and H. J. Zwally, 1999: Deriving long-term time series of sea ice cover from satellite passive-microwave multisensor data sets. *J. Geophys. Res.*, **104**, 15 803–15 814, doi:10.1029/1999JC900081.

Chevallier, M., and D. Salas-Mélia, 2012: The role of the sea ice thickness distribution in the Arctic sea ice potential predictability: A diagnostic approach with a coupled GCM. *J. Climate*, **25**, 3025–3038, doi:10.1175/JCLI-D-11-00209.1.

Comiso, J. C., C. L. Parkinson, R. Gersten, and L. Stock, 2008: Accelerated decline in the Arctic sea ice cover. *Geophys. Res. Lett.*, **35**, L01703, doi:10.1029/2007GL031972.

DeRepentigny, P., B. Tremblay, R. Newton, and S. Pfirman, 2016: Patterns of sea ice retreat in the transition to a seasonally ice-free Arctic. *J. Climate*, doi:10.1175/JCLI-D-15-0733.1, in press.

Deser, C., J. E. Walsh, and M. S. Timlin, 2000: Arctic sea ice variability in the context of the recent atmospheric circulation trends. *J. Climate*, **13**, 617–633, doi:10.1175/1520-0442(2000)013<0617:ASIVIT>2.0.CO;2.

Dethleff, D., P. Loewe, and E. Kleine, 1998: The Laptev Sea flaw lead—Detailed investigation on ice formation and export during 1991/1992 winter season. *Cold Reg. Sci. Technol.*, **27**, 225–243, doi:10.1016/S0165-232X(98)00005-6.

Eisenman, I., W. N. Meier, and J. R. Norris, 2014: A spurious jump in the satellite record: Has Antarctic sea ice expansion been over estimated? *Cryosphere*, **8**, 1289–1296, doi:10.5194/tc-8-1289-2014.

Else, B. G. T., T. N. Papakyriakou, R. Raddatz, R. J. Galley, C. J. Mundy, D. G. Barber, K. Swystun, and S. Rysgaard, 2014: Surface energy budget of landfast sea ice during the transitions from winter to snowmelt and melt pond onset: The importance of net longwave radiation and cyclone forcings. *J. Geophys. Res. Oceans*, **119**, 3679–3693, doi:10.1002/2013JC009672.

Fetterer, F., K. Knowles, W. Meier, and M. Savoie, 2002: (updated daily): Sea ice index. National Snow and Ice Data Center, digital media, accessed October 2014, doi:10.7265/N5QJ7F7W.

Fieguth, P. W., W. C. Karl, A. S. Willsky, and C. Wunsch, 1995: Multiresolution optimal interpolation and statistical analysis of TOPEX/POSEIDON satellite altimetry. *IEEE Trans. Geosci. Remote Sens.*, **33**, 280–292, doi:10.1109/36.377928.

Frey, K. E., G. W. K. Moore, L. W. Cooper, and J. M. Grebmeier, 2015: Divergent patterns of recent sea ice cover across the

Bering, Chukchi, and Beaufort Seas of the Pacific Arctic region. *Prog. Oceanogr.*, **136**, 32–49, doi:10.1016/j.pocean.2015.05.009.

Holland, M. M., and J. Stroeve, 2011: Changing seasonal sea ice predictor relationships in a changing Arctic climate. *Geophys. Res. Lett.*, **38**, L18501, doi:10.1029/2011GL049303.

Hutchings, J. K., and D. K. Perovich, 2015: Preconditioning of the 2007 sea-ice melt in the eastern Beaufort Sea, Arctic Ocean. *Ann. Glaciol.*, **56**, 94–98, doi:10.3189/2015AoG69A006.

Krumpen, T., M. Janout, R. Gerdes, F. Girard-Ardhuin, J. A. Hölemann, and S. Willmes, 2013: Variability and trends in the Laptev Sea ice outflow between 1992–2011. *Cryosphere*, **7**, 349–363, doi:10.5194/tc-7-349-2013.

Kwok, R., 2009: Outflow of Arctic Ocean sea ice into the Greenland and Barents Seas: 1979–2007. *J. Climate*, **22**, 2438–2457, doi:10.1175/2008JCLI2819.1.

——, and D. A. Rothrock, 2009: Decline in Arctic sea ice thickness from submarine and *ICESat* records: 1958–2008. *Geophys. Res. Lett.*, **36**, L15501, doi:10.1029/2009GL039035.

——, and C. Cunningham, 2012: Deformation of the Arctic Ocean ice cover after the 2007 record minimum in summer ice extent. *Cold Reg. Sci. Technol.*, **76-77**, 17–23, doi:10.1016/j.coldregions.2011.04.003.

Lindsay, R. W., J. Zhang, A. J. Schweiger, and M. A. Steele, 2008: Seasonal predictions of ice extent in the Arctic Ocean. *Geophys. Res. Lett.*, **113**, C02023, doi:10.1029/2007JC004259.

Liu, J., M. Song, R. M. Horton, and Y. Hu, 2015: Revisiting the potential of melt pond fraction as a predictor for the seasonal Arctic sea ice extent minimum. *Environ. Res. Lett.*, **10**, 054017, doi:10.1088/1748-9326/10/5/054017.

Meier, W., F. Fetterer, M. Savoie, S. Mallory, R. Duerr, and J. Stroeve, 2013: (updated 2015): NOAA/NSIDC climate data record of passive microwave sea ice concentration, version 2. National Snow and Ice Data Center, accessed February 2016, doi:10.7265/N55M63M1.

Nikolaeva, A. J., and N. P. Sesterikov, 1970: A method of calculation of ice conditions (on the example of the Laptev Sea). *Ice Forecasting Techniques for the Arctic Seas*, B. A. Krutskih, Z. M. Gudkovic, and A. L. Sokolov, Eds., Amerind Publishing, 150–230.

Parkinson, C. L., D. J. Cavalieri, P. Gloersen, H. J. Zwally, and J. C. Comiso, 1999: Arctic sea ice extents, area and trends, 1978–1996. *J. Geophys. Res.*, **104C**, 20 837–20 856, doi:10.1029/1999JC900082.

Perovich, D. K., and C. Polashenski, 2012: Albedo evolution of seasonal Arctic sea ice. *Geophys. Res. Lett.*, **39**, L08501, doi:10.1029/2012GL051432.

——, B. Light, H. Eicken, K. F. Jones, K. Runciman, and S. V. Nghiem, 2007: Increasing solar heating of the Arctic Ocean and adjacent seas, 1979–2005: Attribution and role in the ice–albedo feedback. *Geophys. Res. Lett.*, **34**, L19505, doi:10.1029/2007GL031480.

——, J. A. Richter-Menge, K. F. Jones, and B. Light, 2008: Sunlight, water and ice: Extreme Arctic sea ice melt during the summer of 2007. *Geophys. Res. Lett.*, **35**, L11501, doi:10.1029/2008GL034007.

Persson, P. O. G., 2012: Onset and end of the summer melt season over sea ice: Thermal structure and surface energy perspective from SHEBA. *Climate Dyn.*, **39**, 1349–1371, doi:10.1007/s00382-011-1196-9.

Rampal, P., J. Weiss, and D. Marsan, 2009: Positive trend in the mean speed and deformation rate of Arctic sea ice, 1979–2007. *J. Geophys. Res.*, **114C**, C05013, doi:10.1029/2008JC005066.

Reimnitz, E., D. Dethleff, and D. Nürnberg, 1994: Contrasts in the Arctic shelf sea-ice regimes and some implications: Beaufort Sea versus Laptev Sea. *Mar. Geol.*, **119**, 215–225, doi:10.1016/0025-3227(94)90182-1.

Rigor, I. G., and R. Colony, 1997: Sea-ice production and transport of pollutants in the Laptev Sea, 1979–1993. *Sci. Total Environ.*, **202**, 89–110, doi:10.1016/S0048-9697(97)00107-1.

——, and J. M. Wallace, 2004: Variations in the age of Arctic sea-ice and summer sea-ice extent. *Geophys. Res. Lett.*, **31**, L09401, doi:10.1029/2004GL019492.

——, ——, and R. L. Colony, 2002: Response of sea ice to the Arctic Oscillation. *J. Climate*, **15**, 2648–2663, doi:10.1175/1520-0442(2002)015<2648:ROSITT>2.0.CO;2.

Rösel, A., L. Kaleschke, and G. Birnbaum, 2012: Melt ponds on Arctic sea ice determined from MODIS satellite data using an artificial neural network. *Cryosphere*, **6**, 431–446, doi:10.5194/tc-6-431-2012.

Schröder, D., D. L. Feltham, D. Flocco, and M. Tsamados, 2014: September Arctic sea-ice minimum predicted by spring melt-pond fraction. *Nat. Climate Change*, **4**, 353–357, doi:10.1038/nclimate2203.

Serreze, M. C., and J. Stroeve, 2015: Arctic sea ice trends, variability and implications for seasonal ice forecasting. *Philos. Trans. Roy. Soc. London*, **373**, 20140159, doi:10.1098/rsta.2014.0159.

Smedsrud, L. H., A. Sirevaag, K. Kloster, A. Sorteberg, and S. Sandven, 2011: Recent wind driven high sea ice area export in the Fram Strait contributes to Arctic sea ice decline. *Cryosphere*, **5**, 821–829, doi:10.5194/tc-5-821-2011.

Steele, M., J. Zhang, and W. Ermold, 2010: Mechanisms of summertime upper Arctic Ocean warming and the effect on sea ice melt. *J. Geophys. Res.*, **115**, C11004, doi:10.1029/2009JC005849.

Stroeve, J. C., J. Maslanik, M. C. Serreze, I. Rigor, W. Meier, and C. Fowler, 2011: Sea ice response to an extreme negative phase of the Arctic Oscillation during winter 2009/2010. *Geophys. Res. Lett.*, **38**, L02502, doi:10.1029/2010GL045662.

——, L. C. Hamilton, C. M. Bitz, and E. Blanchard-Wrigglesworth, 2014: Predicting September sea ice: Ensemble skill of the search sea ice outlook 2008–2013. *Geophys. Res. Lett.*, **41**, 2411–2418, doi:10.1002/2014GL059388.

Sumata, H., R. Kwok, R. Gerdes, F. Kauker, and M. Karcher, 2015: Uncertainty of Arctic summer ice drift assessed by high-resolution SAR data. *J. Geophys. Res. Oceans*, **120**, 5285–5301, doi:10.1002/2015JC010810.

Tain-Kunze, X., L. Kaleschke, N. Maaß, M. Mäkynen, N. Serra, M. Drusch, and T. Krumpen, 2014: *SMOS*-derived thin sea ice thickness: Algorithm baseline, product specifications and initial verification. *Cryosphere*, **8**, 997–1018, doi:10.5194/tc-8-997-2014.

Thorndike, A. S., and R. Colony, 1982: Sea ice motion in response to geostrophic winds. *J. Geophys. Res.*, **87**, 5845–5852, doi:10.1029/JC087iC08p05845, doi:10.1029/JC087iC08p05845.

Timohkov, L. A., 1994: Regional characteristics of the Laptev and the East Siberian Seas: Climate, topography, ice phases, thermohaline regime, circulation. *Russian-German Cooperation in the Siberian Shelf Seas: Geo-System Laptev Sea*, H. Kassens et al., Eds., Alfred Wegener Institute for Polar and Marine Research, 15–31.

Travers, C., and R. Woodgate, 2012: Quantifying sea-ice volume flux using moored instrumentation in the Bering Strait. M.S. thesis, College of the Environment, School of Oceanography, University of Washington, 77 pp.

Tschudi, M., C. Fowler, J. Maslanik, J. S. Stewart, and W. Meier, 2016: Polar pathfinder daily 25 km ease-grid sea ice motion vectors, version 3. National Snow and Ice Data Center Distributed Active Archive Center, accessed February 2016, doi:10.5067/O57VAIT2AYYY.

Tucker, W. B., J. W. Weatherly, D. T. Eppler, L. D. Farmer, and D. L. Bentley, 2001: Evidence for rapid thinning of sea ice in the western Arctic Ocean at the end of the 1980s. *Geophys. Res. Lett.*, **28**, 2851–2854, doi:10.1029/2001GL012967.

Wang, J., J. Zhang, E. Watanabe, M. Ikeda, K. Mizobata, J. E. Walsh, X. Bai, and B. Wu, 2009: Is the dipole anomaly a major driver to record lows in Arctic summer sea ice extent? *Geophys. Res. Lett.*, **36**, L05706, doi:10.1029/2008GL036706.

Woodgate, R. A., T. Weingartner, and R. Lindsay, 2010: The 2007 Bering Strait oceanic heat flux and anomalous Arctic sea-ice retreat. *Geophys. Res. Lett.*, **37**, L01602, doi:10.1029/2009GL041621.

Zhang, X., J. E. Walsh, J. Zhang, U. S. Bhatt, and M. Ikeda, 2004: Climatology and interannual variability of Arctic cyclone activity: 1948–2002. *J. Climate*, **17**, 2300–2317, doi:10.1175/1520-0442(2004)017<2300:CAIVOA>2.0.CO;2.